ChemPhysMater 3 (2024) 220–229

Contents lists available at ScienceDirect

ChemPhysMater

journal homepage: https://www.keaipublishing.com/en/journals/chemphysmater/

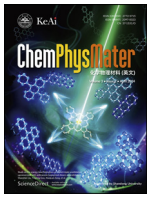

Research Article

Flower-like Fe-doped $NiSe_2$/C hybrid spheres fabricated by a glucose-intercalation strategy for enhanced sodium storage properties

Cheng Liu[a], Yi Wen[a], Gaoya Ren[a], Yaxuan Li[a], Qianqian Sun[a], Shenghui Shen[a], Zhujun Yao[a], Yefeng Yang[a,b,*]

[a] School of Materials Science and Engineering, Zhejiang Sci-Tech University, Hangzhou 310018, China
[b] Institute of Wenzhou, Zhejiang University, Wenzhou 325036, China

ARTICLE INFO

Keywords:
Glucose-intercalation
Fe-doped $NiSe_2$
Carbon nanosheets
Sodium-ion batteries

ABSTRACT

Nickel diselenide ($NiSe_2$), which has a high theoretical capacity, has attracted considerable attention as a promising anode material for sodium-ion batteries (SIBs). Nevertheless, the intrinsically low conductivity, large volume variation, and significant aggregation of $NiSe_2$ during sodiation/desodiation remain significant obstacles to its application. Herein, we report flower-like Fe-doped $NiSe_2$/C hybrid spheres (denoted as Fe-$NiSe_2$/C) fabricated by a glucose intercalation strategy for efficient sodium storage. These Fe-$NiSe_2$/C hybrid spheres are composed of thin porous carbon nanosheets decorated with Fe-$NiSe_2$ nanoparticles. In situ introduced carbon nanosheets derived from intercalated glucose accompanied by moderate Fe doping in $NiSe_2$ nanoparticles can provide accelerated ion/electron transfer kinetics through fast ion channels in the flower-like architecture and intimately contacted interfaces between $NiSe_2$ and carbon nanosheets as well as maintain structural integrity by alleviating volume variation. Consequently, the optimal anode of the Fe-$NiSe_2$/C hybrid spheres delivered a high discharge capacity of 415 mAh g^{-1} at 0.5 A g^{-1}, outstanding rate capability (243 mAh g^{-1} at 5 A g^{-1}), and significantly enhanced cycling stability (388 mAh g^{-1} at 1 A g^{-1} over 200 cycles). This work offers an efficient and valuable strategy for realizing tailored heteroatom doping in transition metal selenides, accompanied by an in situ combination of conductive carbonaceous networks for advanced alkali metal ion batteries.

1. Introduction

With the growing global demand for large-scale and reliable energy storage devices, the past decade has witnessed the rapid development of rechargeable sodium-ion batteries (SIBs) featuring the advantages of the high natural abundance, wide distribution, and low price of sodium on Earth as well as nearly compatible manufacturing technologies with those for the current mainstream lithium-ion batteries (LIBs) [1–8]. However, the unsatisfactory reaction kinetics, fast capacity degradation, and inferior rate capability mainly induced by the larger ionic radius of Na^+ (1.02 Å) as well as the drastic volume variation of electrode materials during the repeated sodiation/desodiation process greatly hinder the practical application prospects of SIBs [9,10]. Regarding the notable progress achieved in the field of cathode materials ranging from layered oxides to polyanionic compounds and Prussian blue analogs (PBAs), the choice of anode materials is relatively limited, and research still remains in its infancy [11–13]. Consequently, the development of suitable anode materials with enhanced sodium storage performance to meet the requirements of SIBs is urgently needed.

To date, much research effort has been devoted to high-capacity conversion-type materials (i.e., metal sulfides [14,15], selenides [16–21], and phosphides [22,23]) as promising anodes as well as widely studied carbonaceous anodes. Among them, nickel diselenide ($NiSe_2$) has aroused increasing attention because of its relatively high theoretical capacity (495 mAh g^{-1}), suitable working potential for sodium storage, and higher conductivity than its oxide/sulfide counterparts [24–26]. However, the sluggish kinetics of conversion reactions, serious pulverization/aggregation related to large volume variations, and shuttling effect of polyselenides formed during the cycling process usually give rise to fast capacity degradation and poor rate capability [27]. To mitigate these intractable issues, some feasible methods have been employed to improve the sodium storage performance of $NiSe_2$, such as morphology control [28,29], integration of conductive materials [30–34], heteroatom doping [35,36], and heterostructure engineering [37–42]. Heteroatom doping of certain elements is a feasible and versatile method because it can effectively modulate the electronic structure and enhance the conductivity and electrochemical activity, thereby accelerating the reaction kinetics [43]. For instance, Xu et al. reported Co doping in

* Corresponding author.
E-mail address: yangyf@zstu.edu.cn (Y. Yang).

https://doi.org/10.1016/j.chphma.2024.01.004
Received 27 September 2023; Received in revised form 15 December 2023; Accepted 2 January 2024
Available online 2 February 2024
2772-5715/© 2024 The Authors. Publishing Services by Elsevier B.V. on behalf of KeAi Communications Co. Ltd. This is an open access article under the CC BY-NC-ND license (http://creativecommons.org/licenses/by-nc-nd/4.0/)

$NiSe_2$ and realized the fabrication of coral-like hierarchical $Ni_xCo_{1-x}Se_2$ delivering a capacity of 321 mAh g^{-1} after 2000 cycles at 2 A g^{-1}, which was mainly attributed to the enhanced conductivity by Co doping in $NiSe_2$ [44]. In another work, Li et al. demonstrated the fabrication of Co-doped $NiSe_2$/C hybrid nanosheets with good long-term cycling stability (306 mAh g^{-1} after 5000 cycles at 5 A g^{-1}) and elucidated the sodium storage mechanism of the reversible phase transition occurring in Co-doped $NiSe_2$ through ex situ X-ray diffraction (XRD) analysis [35]. More recently, Geng et al. illustrated the Fe doping of $NiSe_2$ nanosheets through the selenization of an Fe–Ni binary metal-organic framework (MOF) as a template. Owing to the occurrence of more electroactive sites and enhanced conductivity originating from Fe doping in $NiSe_2$, the as-prepared Fe-doped $NiSe_2$@C exhibited a capacity of 302 mA h g^{-1} at 5 A g^{-1} after 1000 cycles [36]. Unfortunately, many of these previously reported methods involve complex preparation processes, and controllable heteroatom doping of $NiSe_2$ with simultaneous carbon integration remains a significant challenge.

Herein, we propose flower-like Fe-doped $NiSe_2$/C hybrid spheres (denoted as Fe-$NiSe_2$/C) derived from a glucose-intercalation strategy consisting of porous thin carbon nanosheets decorated with Fe-$NiSe_2$ nanoparticles that enable both a high rate capacity and enhanced cycling stability of SIBs. In our design, the precursors of glucose-intercalated and Fe-doped $Ni(OH)_2$ flower-like spheres (denoted as Fe-$Ni(OH)_2$-G) were synthesized by the in situ introduction of a carbon source (glucose) and Fe doping using a facile one-pot hydrothermal method, and the targeted Fe-$NiSe_2$/C composite with a flower-like structure was obtained through a successive carbonization/selenization combined process. Glucose and other small molecules can be readily intercalated into layered nickel-based hydroxides under mild reaction conditions with increased interlayer spacing [45–48]. Inspired by this fact, we suggest that in situ introduced carbon nanosheets derived from intercalated glucose accompanied by moderate Fe doping in $NiSe_2$ nanoparticles can effectively enhance the electrical conductivity of $NiSe_2$ with a tuned electronic structure, ensure intimately contacted interfaces between the carbon nanosheets and $NiSe_2$, provide more favorable channels for ion diffusion in the flower-like architecture, and maintain structural integrity with alleviated volume expansion/shrinkage. Consequently, the resulting optimal Fe-$NiSe_2$/C hybrid spheres delivered a high discharge capacity, outstanding rate capability, and significantly enhanced cycling stability.

2. Results and discussion

Fig. 1 shows the detailed synthetic procedure for flower-like Fe-$NiSe_2$/C hybrid spheres. First, flower-like Fe-$Ni(OH)_2$-G hybrid spheres were synthesized as precursors *via* a facile one-pot hydrothermal method using nickel nitrate, iron nitrate, urea, ammonium fluoride, and glucose as starting materials. Notably, as the carbon source, glucose molecules can be spontaneously intercalated into the in situ formed interlayer structure of Fe-$Ni(OH)_2$ spheres [49], whereas the addition of NH_4F to the reaction can facilitate the formation of sheet-like structured hydroxides with enhanced crystallinity [50,51]. The Fe-$Ni(OH)_2$-G precursor was subjected to a two-step thermal treatment involving successive carbonization and selenization, generating the targeted flower-like Fe-$NiSe_2$/C hybrid spheres. During this process, the intercalated glucose was transformed into thin interlaced carbon nanosheets, and Fe-$Ni(OH)_2$ was simultaneously converted into Fe-$NiSe_2$ nanoparticles tightly anchored on the carbon nanosheets, with the flower-like morphology basically maintained. By varying the feeding amount of iron nitrate ($x = 0$, 0.2 and 0.4 mmol), a series of flower-like hybrid spheres was obtained, which were labeled as $NiSe_2$/C, 0.1Fe-$NiSe_2$/C and 0.2Fe-$NiSe_2$/C, respectively.

To confirm the intercalation of glucose within the layered precursors, the XRD patterns of $Ni(OH)_2$, $Ni(OH)_2$-G, 0.1Fe-$Ni(OH)_2$-G, and 0.2Fe-$Ni(OH)_2$-G were compared, as shown in Fig. S1. Pristine $Ni(OH)_2$ clearly belongs to the β-$Ni(OH)_2$ phase (JCPDS No. 14–0117) [52,53]. After the introduction of glucose into the reaction, all the characteristic peaks arising from β-$Ni(OH)_2$ completely disappeared in the $Ni(OH)_2$-G, 0.1Fe-$Ni(OH)_2$-G, and 0.2Fe-$Ni(OH)_2$-G precursors, while a series of new diffraction peaks attributed to the α-$Ni(OH)_2$ phase (JCPDS No. 38–0715) emerged [54]. α-$Ni(OH)_2$ typically exhibits a distinctly larger interlayer distance of 0.75 nm compared with that (0.46 nm) of β-$Ni(OH)_2$, reflecting the successful intercalation of glucose into the layered hydroxide precursors, similar to the cases previously reported in the literature [55,56].

The introduction of glucose and different amounts of iron nitrate significantly affected the formation of Fe-$NiSe_2$/C hybrid spheres with modulated morphologies and structures. Figs. 2(a)–(c) display the flower-like morphologies of the $NiSe_2$/C, 0.1Fe-$NiSe_2$/C and 0.2Fe-$NiSe_2$/C hybrid spheres with very similar average diameters of approximately 4 μm, consisting of many interlaced nanosheets with rough surfaces. The average thickness of the nanosheets in these samples was estimated to be approximately 40 nm, which is slightly larger than that (30 nm) of pristine $NiSe_2$ derived from the reaction without the introduction of glucose, as shown in Fig. S2. Moreover, as the amount of iron nitrate introduced into the reaction increased from 0 to 0.2 and 0.4 mmol, the interlaced nanosheets in the samples of $NiSe_2$/C, 0.1Fe-$NiSe_2$/C, and 0.2Fe-$NiSe_2$/C become rougher and more densely packed with obviously decreased lateral size from 4 to 1.5 and 1 μm, respectively. In addition, a large number of small nanoparticles and penetrating pores are clearly observed in the nanosheets, especially in the 0.1Fe-$NiSe_2$/C and 0.2Fe-$NiSe_2$/C samples, which are expected to expose more electroactive sites, facilitate electrolyte infiltration, and accelerate ion diffusion kinetics. Fig. 2(d) compares the XRD patterns of $NiSe_2$/C, 0.1Fe-$NiSe_2$/C, and 0.2Fe-$NiSe_2$/C, illustrating the structural changes upon the addition of iron salt. For the $NiSe_2$/C sample, all the characteristic peaks located at 30.1°, 33.6°, 37.0°, 50.9°, 55.6°, and 57.9° can be indexed to the (220), (210), (211), (311), (230), and (321) planes of cubic-phase $NiSe_2$ (JCPDS No. 11–0552) [57], and no signals arising from carbon species were identified, implying the amorphous characteristic of carbon in the hybrid spheres. Upon increasing the amount of iron salt introduced into the reaction, all the diffraction peaks were found to

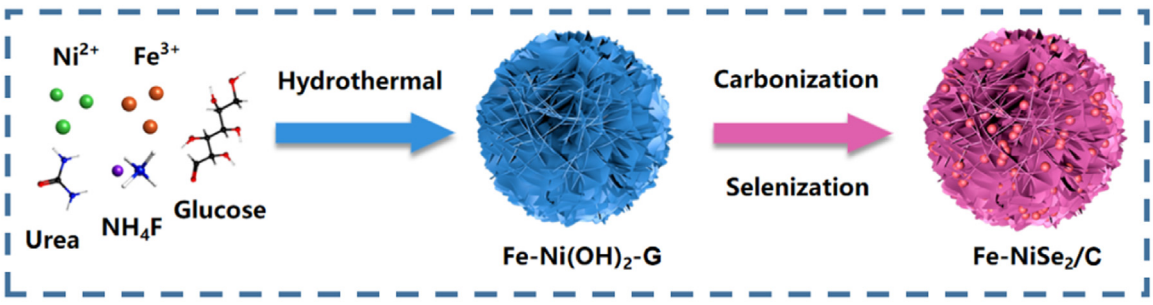

Fig. 1. Schematic diagram showing the fabrication procedure of flower-like Fe-$NiSe_2$/C hybrid spheres.

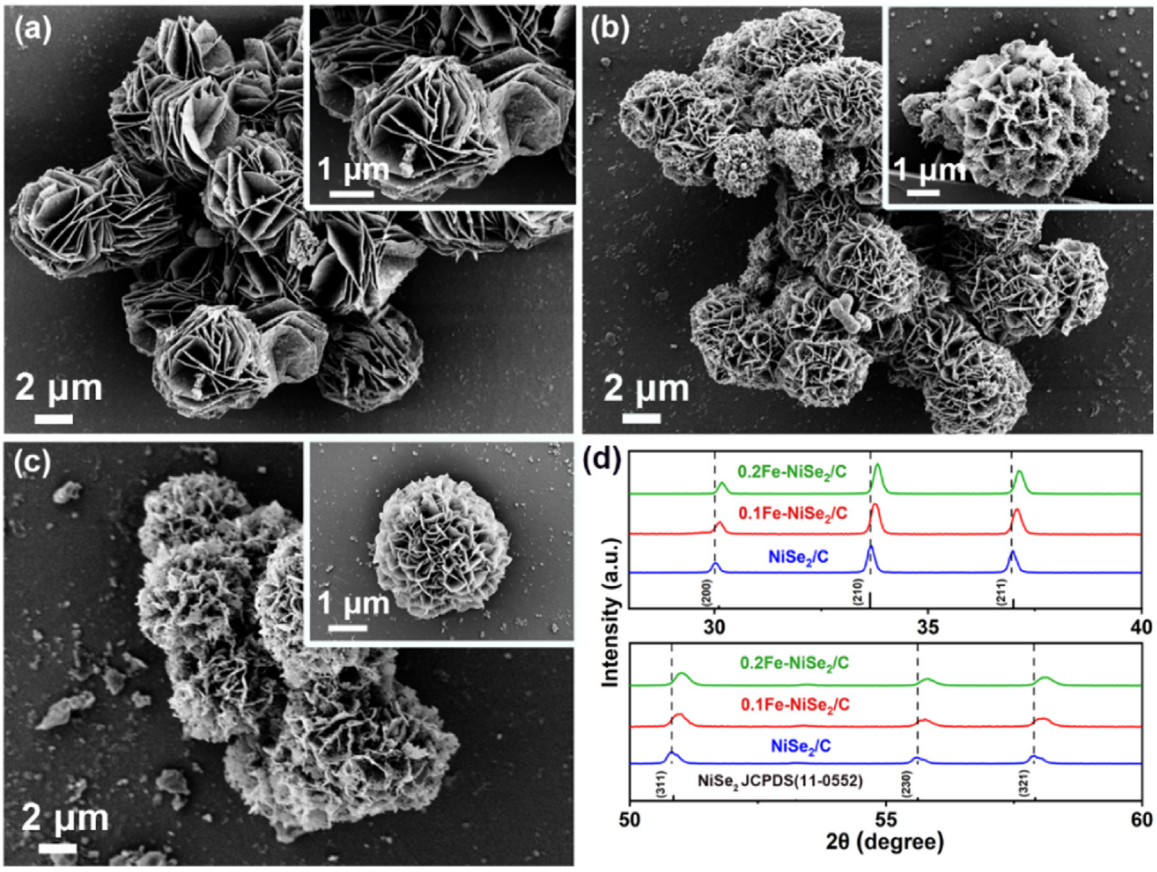

Fig. 2. Typical scanning electron microscopy (SEM) images of (a) $NiSe_2$/C, (b) 0.1Fe-$NiSe_2$/C, and (c) 0.2Fe-$NiSe_2$/C at low- and high-magnifications and (d) corresponding XRD patterns.

shift gradually toward higher angles, which was likely associated with the lattice substitution of Ni in $NiSe_2$ by Fe ions possessing a smaller ionic radius than that of Ni ions, reflecting the successful doping of Fe species in $NiSe_2$. Detailed energy dispersive spectroscopy (EDS) characterization of the 0.1Fe-$NiSe_2$/C and 0.2Fe-$NiSe_2$/C samples indicated that the practical Fe doping contents of Fe/(Fe+Ni) were 15.0 atom% and 24.4 atom%, respectively, as summarized in Table S1. Considering the superior Na storage properties of the 0.1Fe-$NiSe_2$/C hybrid spheres, much emphasis should be placed on this sample to illustrate its appealing compositional and structural merits.

The composition and surface chemical states of 0.1Fe-$NiSe_2$/C on the surface were analyzed using X-ray photoelectron spectroscopy (XPS). The survey XPS spectrum shown in Fig. S3 verifies that the composite primarily consisted of Ni, Fe, Se, C, and O. The relatively strong oxygen signal in Fig. S3 is most likely due to the partial oxidation of metal selenides during sample processing [58]. As shown in Fig. 3(a), the Ni 2p high-resolution XPS spectrum exhibits four peaks located at 852.4, 853.8, 869.8, and 871.6 eV, which are references to Ni^{2+} $2p_{3/2}$, Ni^{3+} $2p_{3/2}$, Ni^{2+} $2p_{1/2}$, and Ni^{3+} $2p_{1/2}$, respectively, along with their two satellite peaks at 857.8 and 875.5 eV, confirming the presence of mixed Ni^{2+} and Ni^{3+} ions in the 0.1Fe-$NiSe_2$/C sample [40,42]. Similarly, the Fe 2p high-resolution spectrum (Fig. 3(b)) can be deconvoluted into two sets of characteristic peaks centered at 710.3/723.2/717.3 eV and 712.1/725.5/729.3 eV, respectively, relating to the Fe $2p_{3/2}$ and Fe $2p_{1/2}$ mixed oxidation states in the sample [59,60]. The high-resolution Se 3d XPS spectrum (Fig. 3(c)) reveals two fitted peaks at the binding energies of 54.0 and 54.9 eV attributed to Se $3d_{5/2}$ and Se $3d_{3/2}$ of the metal-Se bond, and the broad peak at 56.6 eV is correlated with the surface oxidation state of Se species [61,62]. Regarding the C 1s XPS spectrum (Fig. 3(d)), four deconvoluted peaks centered at 283.1, 284.5, 285.4, and 288.5 eV exist, corresponding to C–Ni, C–C/C=C, C–O, and C=O bonds, respectively [63]. Meanwhile, the appearance of the C–Ni bond might imply the existence of interfacial interactions between the Fe-$NiSe_2$ nanoparticles and carbon nanosheets [64,65]. We suggest that the C–Ni bond can act as a functional bridge to improve the electron/ion transport ability and effectively enhance the structural integrity of the hybrid spheres by inhibiting the agglomeration of active materials.

The internal microstructures of the 0.1Fe-$NiSe_2$/C hybrid spheres were investigated using transmission electron microscopy (TEM). Fig. 4(a) shows the representative TEM image of an individual 0.1Fe-$NiSe_2$/C hybrid sphere with a diameter of approximately 4 μm, which shows that the flower-like spherical structure is mainly composed of massive interlaced carbon nanosheets with distinct wrinkled features. The magnified TEM image (Fig. 4(b)) shows that these thin carbon nanosheets were densely decorated with a large number of tiny Fe-$NiSe_2$ nanoparticles with sizes in the range of 10–20 nm. The high resolution TEM (HRTEM) images acquired from different regions (Figs. 4(c)(d)) reveal a series of well-resolved lattice fringes separated by 0.23, 0.20, and 0.18 nm, corresponding well to the (211), (220), and (311) crystal planes of $NiSe_2$ phase (JCPDS No. 11–0552), respectively, which is in good accordance with the concentric diffraction rings from the selected area electron diffraction (SAED) pattern, as depicted in Fig. S4 [66,67]. Furthermore, Fig. 4(e) shows a high-angle annular dark-field (HAADF) scanning TEM (STEM) image, further confirming the flower-like morphology of the 0.1Fe-$NiSe_2$/C hybrid spheres consisting of numerous interlaced wrinkled nanosheets. The EDS mapping analysis demonstrated that the strong overlapping signals of Ni, Fe, and Se are uniformly distributed in the hybrid spheres, while C with a weak signal was identified from the entire selected area, suggesting the presence of numerous Fe-$NiSe_2$ nanoparticles tightly anchored and covering the surface of

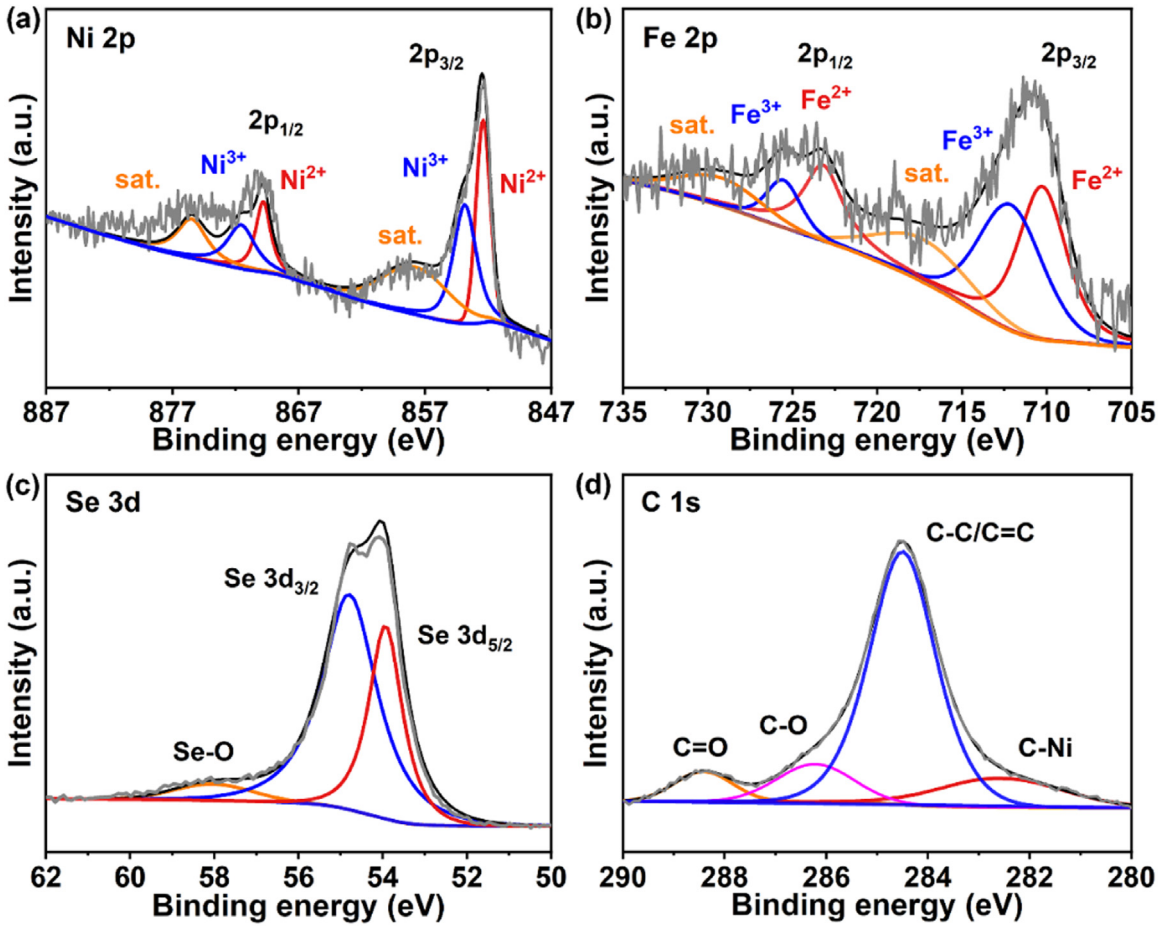

Fig. 3. XPS high resolution spectra of 0.1Fe-$NiSe_2$/C: (a) Ni 2p, (b) Fe 2p, (c) Se 3d, and (d) C 1s, respectively.

the carbon nanosheets. Such a unique heterostructured architecture not only promotes the rapid penetration and diffusion of electrolyte ions but also effectively facilitates electron transfer in the hybrid spheres, highly benefitting high-rate sodium storage.

The electrochemical performance of the 0.1Fe-$NiSe_2$/C hybrid spheres as SIB anodes was first evaluated by assembling and testing them in a standard CR2025 coin-type half-cell. Fig. 5(a) shows the cyclic voltammetry (CV) curves for the 0.1Fe-$NiSe_2$/C electrode measured at a scan rate of 0.1 mV s^{-1} between 0.01 and 3 V (vs. Na^+/Na). In detail, three distinct reduction peaks located at approximately 1.24, 1.00, and 0.58 V are clearly observed in the first cathodic scan, which can be attributed to the insertion of Na^+ into $NiSe_2$ to generate Na_xNiSe_2, further conversion reaction of Na_xNiSe_2 to form metallic Ni and Na_2Se, and formation of a solid electrolyte interphase (SEI) film, respectively [34]. In the corresponding anodic scan, two sharp oxidation peaks are observed at 1.76 and 1.89 V, correlating to the desodiation process [26,32]. During the second cycle, the reduction peak at 0.58 V completely disappears, and the peaks at 1.00 and 1.24 V shift to higher voltages of 1.12 and 1.46 V, while the two oxidation peaks at 1.76 and 1.89 V move to lower voltages of 1.74 and 1.85 V, which might be caused by the structural rearrangement and activation of active materials during cycling [18]. From the second cycle onward, all the CV curves substantially overlapped, indicating good electrochemical reversibility and structural stability of the 0.1Fe-$NiSe_2$/C electrode. Fig. 5(b) presents the galvanostatic charge discharge (GCD) curves of the 0.1Fe-$NiSe_2$/C electrode tested at 1 A g^{-1}, delivering a discharge/charge capacity of 804/548 mAh g^{-1} in the first cycle and showing an initial Coulombic efficiency (ICE) of approximately 68.2 %. The obvious irreversible capacity loss is likely due to the partial decomposition and consumption of the electrolyte, accompanied by the establishment of an SEI film over the electrode with a large surface area [68,69]. Fig. 5(b) shows that the CE value of the 0.1Fe-$NiSe_2$/C electrode quickly increased from 68.2% to 96.5% during the second cycle and then remained stable at approximately 99% in subsequent cycles. Fig. 5(c) compares the cycling performance of 0.1Fe-$NiSe_2$/C with pristine $NiSe_2$, $NiSe_2$/C, and 0.2Fe-$NiSe_2$/C electrodes at 1 A g^{-1}. As expected, the 0.1Fe-$NiSe_2$/C electrode exhibited a high discharge capacity of 388 mAh g^{-1} with 71.7% retention (to the third cycle) after 200 cycles, which is much superior to the values of pristine $NiSe_2$ (85 mAh g^{-1}), $NiSe_2$/C (286 mAh g^{-1}) and 0.2Fe-$NiSe_2$/C (217 mAh g^{-1}), showing the enhanced sodium storage capacity and cycling stability of the 0.1Fe-$NiSe_2$/C electrode. Moreover, SEM images of the 0.1 Fe-$NiSe_2$/C electrode after 200 cycles at 1 A g^{-1} were also obtained, as shown in Fig. S5, which indicate that the flower-like morphology and microstructure of the 0.1Fe-$NiSe_2$/C electrode was nearly retained. The rate performance of the 0.1Fe-$NiSe_2$/C electrode tested under varied current densities is shown in Fig. 5(d) and compared with those of pristine $NiSe_2$, $NiSe_2$/C, and 0.2Fe-$NiSe_2$/C. For the 0.1Fe-$NiSe_2$/C electrode, high average discharge capacities of 415, 376, 328, and 243 mAh g^{-1} can be achieved at current densities of 0.5, 1, 2, and 5 A g^{-1}, respectively, which are much higher than those of pristine $NiSe_2$ (222/113/82/57 mAh g^{-1}), $NiSe_2$/C (331/302/257/188 mAh g^{-1}), and 0.2Fe-$NiSe_2$/C (284/250/216/175 mAh g^{-1}) at corresponding current densities. Additionally, the discharge capacity of the 0.1Fe-$NiSe_2$/C electrode can still recover quickly to 308, 332, and 341 mAh g^{-1}, respectively, when the current density is reset to 2, 1, and 0.5 A g^{-1} in steps, corroborating the much better rate capability. The obtained results indicate a significantly improved electrochemical performance of the 0.1Fe-$NiSe_2$/C electrode, which is comparable to or even outper-

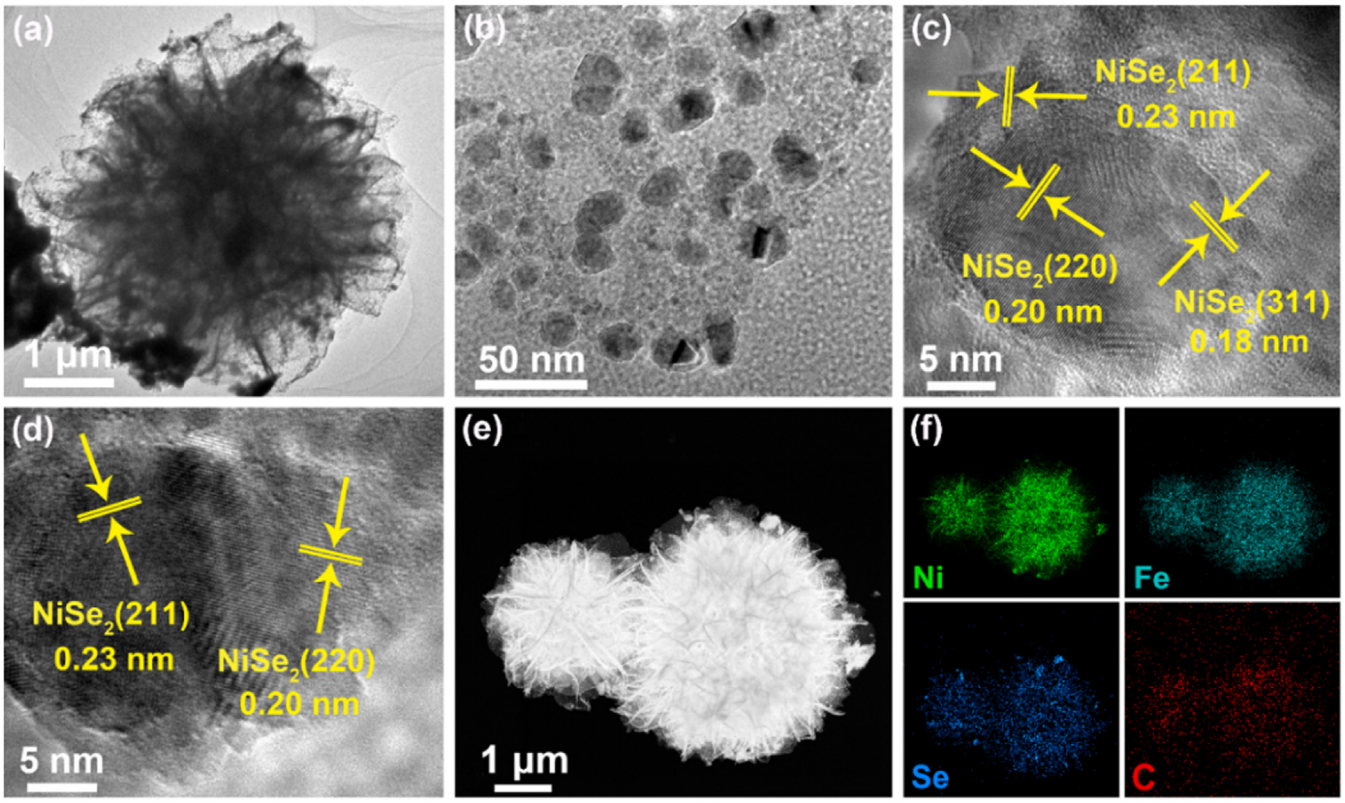

Fig. 4. (a)(b) Low- and high-magnification TEM images of a 0.1Fe-$NiSe_2$/C hybrid sphere, (c)(d) HRTEM images, (e) HAADF-STEM image, and (f) EDS elemental mapping images of Ni, Fe, Se, and C.

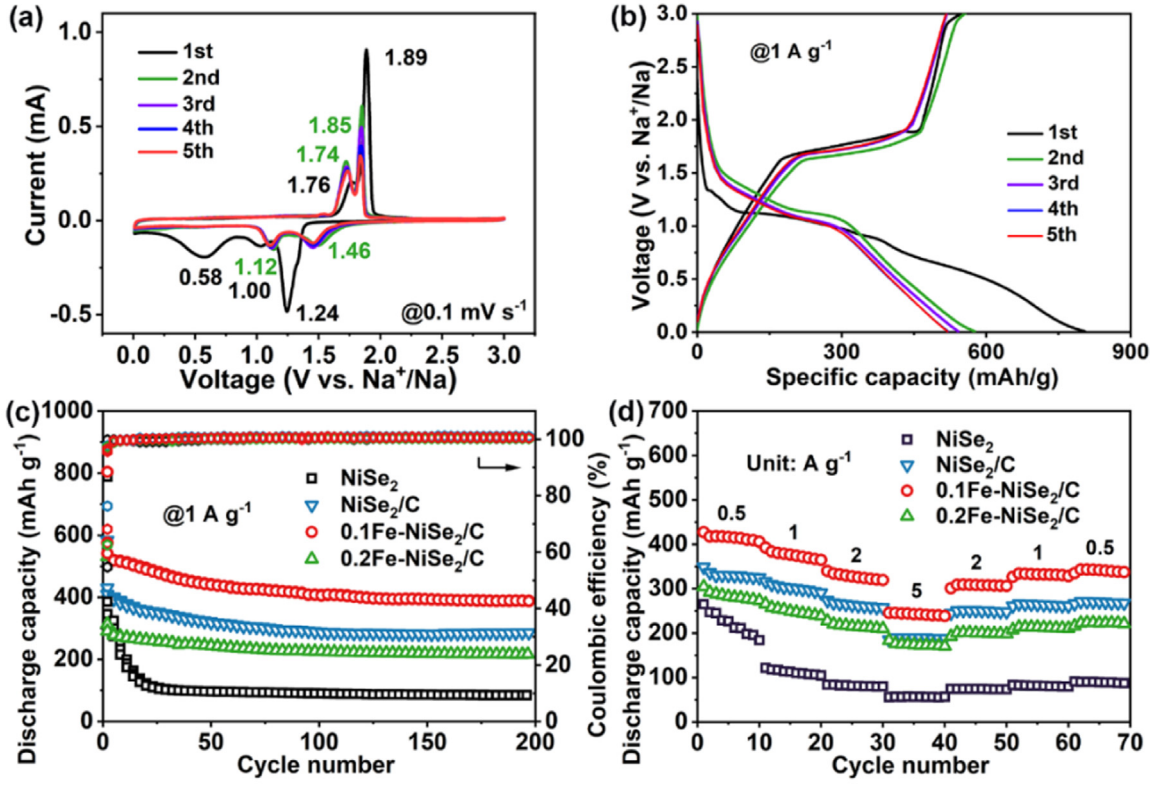

Fig. 5. Electrochemical performance of the 0.1Fe-$NiSe_2$/C in half-cell: (a) first five CV curves, (b) first five GCD curves, comparison of the (c) cycling performance and (d) rate capability of the $NiSe_2$, $NiSe_2$/C, 0.1Fe-$NiSe_2$/C, and 0.2Fe-$NiSe_2$/C electrodes.

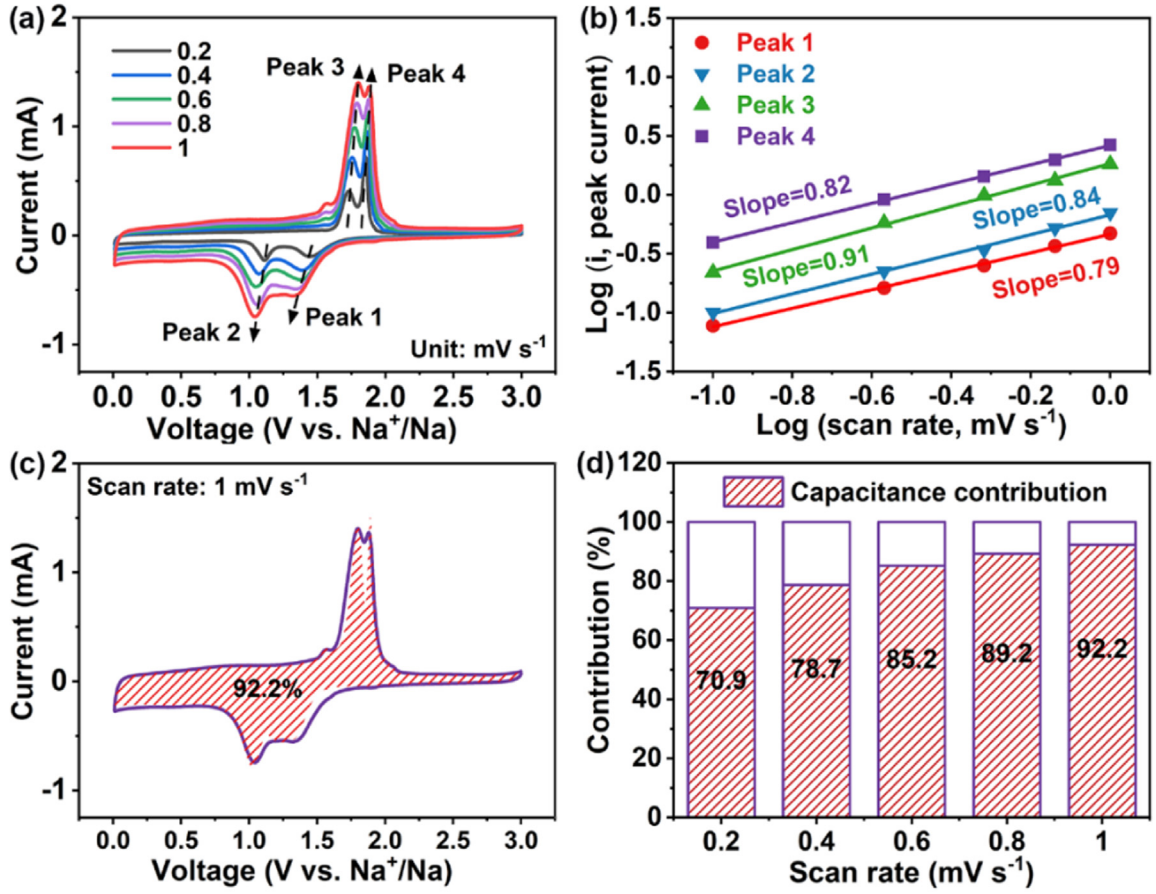

Fig. 6. (a) CV curves of the 0.1Fe-$NiSe_2$/C electrode at different scan rates, (b) log(i) vs. log(v) plots for each redox peak, (c) capacitive contribution at 1.0 mV s^{-1}, and (d) capacitive contribution proportions at different scan rates.

forms those of pristine $NiSe_2$, $NiSe_2$/C, 0.2Fe-$NiSe_2$/C, and other recently reported $NiSe_2$-based anodes for SIBs, as listed in Table S2.

Notably, the capacity of 0.2Fe-$NiSe_2$/C is much lower than those of 0.1Fe-$NiSe_2$/C and $NiSe_2$, implying that an optimum amount of Fe doping in $NiSe_2$ exists to achieve the best sodium storage properties, which is probably attributed to the modulated electronic structure of $NiSe_2$ induced by Fe doping. We suggest that the heteroatom doping of Fe at a suitable concentration in $NiSe_2$ and in situ combination with highly conductive carbon nanosheets derived from intercalated glucose can mutually contribute to the improved sodium storage performance of the 0.1Fe-$NiSe_2$/C electrode. Moreover, as shown in Fig. S6, the XRD pattern of the 0.1Fe-$NiSe_2$/C electrode at the full discharge state of 0.01 V reveals a series of distinct diffraction peaks at 22.8°, 37.5°, 44.1°, 53.9°, and 59.1° attributed to the (111), (220), (311), (400), and (331) planes of Na_2Se (JCPDS No. 47–1699), which are accompanied by several peaks located at 39.0°, 41.5°, 44.5°, and 58.4° arising from the (010), (002), (011), and (012) of metallic Ni (JCPDS No. 45–1027), clearly confirming the occurrence of the conversion reaction in the electrode [26,36,42].

Considering the outstanding sodium storage performance of the 0.1Fe-$NiSe_2$/C electrode, detailed reaction kinetics were investigated using CV analysis. Fig. 6(a) displays the CV curves of the 0.1Fe-$NiSe_2$/C electrode tested from 0.2 to 1.0 mV s^{-1}, showing very similar contours. The sodium storage mechanism generally involving surface capacitive and diffusion-controlled processes can be elucidated from the CV curves by the relationship between the peak current (i) and scan rate (v), which obeys the power-law equation [70,71]:

$$i = av^b,$$

where b is derived from the slope of the linear fit of log(i) versus log(v). Typically, a b-value of 1 or 0.5 is indicative of a complete surface capacitive or diffusion-controlled process. Fig. 6(b) shows that the b-values for the four selected redox peaks are 0.79, 0.84, 0.91, and 0.82, indicating a hybrid sodium storage mechanism in the 0.1Fe-$NiSe_2$/C electrode. Moreover, the corresponding contributions to the total capacity at a fixed potential were quantified using the following equation [72,73]:

$$i = k_1 v + k_2 v^{1/2},$$

where $k_1 v$ and $k_2 v^{1/2}$ represent the current responses of the capacitive- and diffusion-controlled contributions, respectively. Fig. 6(c) shows the surface capacitive contribution of the 0.1Fe-$NiSe_2$/C electrode at 1 mV s^{-1}, which accounts for 92.2% of the total capacity, as indicated by the shaded area. When the scan rate was gradually increased from 0.2 to 1 mV s^{-1}, the proportion of the capacitive contribution progressively increased from 70.9% to 78.7%, 85.2%, 89.2%, and 92.2%, as shown in Fig. 6(d). The relatively high proportion of the capacitive contribution indicates the fast transport kinetics of Na^+, which is highly conducive to achieving outstanding rate capability and cycling stability.

In addition, the charge-transport kinetics of the electrodes were further investigated using electrochemical impedance spectroscopy (EIS) spectra recorded at different cycles. For the obtained Nyquist plots (Figs. 7(a)–(c)), each profile features a semicircle in the high-frequency region and a sloped line in the low-frequency region, representing the charge-transfer resistance (R_{ct}) at the electrode/electrolyte interface and the Warburg impedance (Z_w) correlated to Na^+ diffusion [74], respectively. Fig. 7(a) depicts the Nyquist plots of the $NiSe_2$, $NiSe_2$/C, 0.1Fe-$NiSe_2$/C, and 0.2Fe-$NiSe_2$/C electrodes measured at an open-circuit

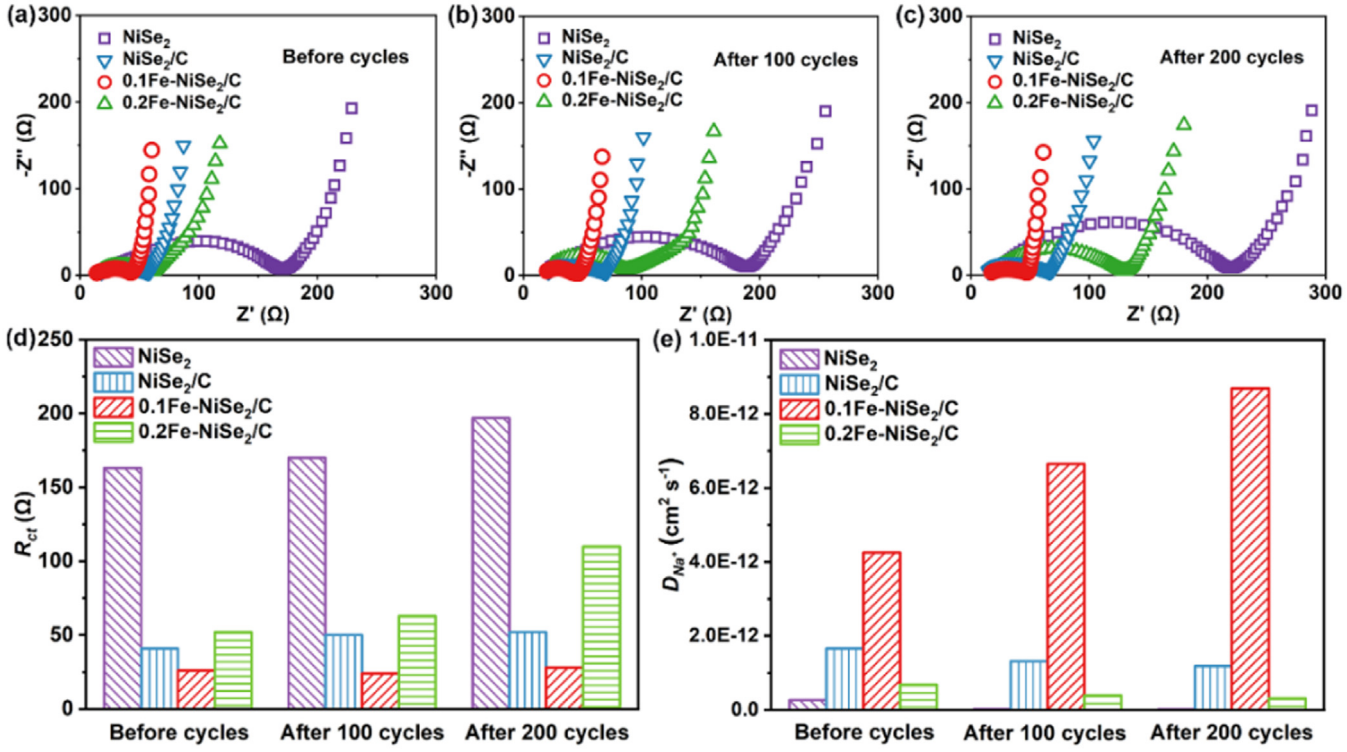

Fig. 7. (a)–(c) Nyquist plots of the $NiSe_2$, $NiSe_2$/C, 0.1Fe-$NiSe_2$/C, and 0.2Fe-$NiSe_2$/C electrodes: before cycling, after 100 cycles, and after 200 cycles at 0.2 A g^{-1}, (d)(e) corresponding variation of the R_{ct} and D_{Na^+}.

voltage (OCV) state, while Figs. 7(b)(c) display the Nyquist plots of these electrodes in the fully charged state after 100 and 200 cycles under 0.2 A g^{-1}, respectively. By fitting the Nyquist plots using the equivalent circuit model (Fig. S7), the R_{ct} values of the electrodes at different cycles were derived, as depicted in Fig. 7(d). Specifically, the 0.1Fe-$NiSe_2$/C electrode exhibits a much lower R_{ct} of 26 Ω before cycling compared with those of $NiSe_2$ (163 Ω), $NiSe_2$/C (41 Ω), and 0.2Fe-$NiSe_2$/C (52 Ω). The flower-like structure composed of interlaced thin carbon nanosheets is speculated to greatly promote charge transfer at the electrode/electrolyte interface and effectively reduce the R_{ct}, resulting in an enhanced charge transfer ability of $NiSe_2$/C compared to that of pristine $NiSe_2$. Meanwhile, an appropriate amount of Fe doping in $NiSe_2$/C further improved the conductivity and minimized the R_{ct}. As the cycling proceeding to 100 and 200 cycles, the R_{ct} values of the pristine $NiSe_2$, $NiSe_2$/C, 0.1Fe-$NiSe_2$/C, and 0.2Fe-$NiSe_2$/C electrodes progressively increased to 170/197, 50/52, 24/28, and 63/110 Ω, respectively. We suggest that the aggregation and structural collapse of active materials might occur on the surface of the electrodes to different degrees, which deteriorates the charge transfer process during cycling with increased R_{ct} results. This phenomenon was quite obvious for the pristine $NiSe_2$ and 0.2Fe-$NiSe_2$/C electrodes, possibly because of the lack of an in situ combination of carbon nanosheets interlaced with $NiSe_2$ and excess Fe doping.

Moreover, a quantitative examination of the Na^+ diffusion coefficient (D_{Na^+}) can be achieved from the low-frequency region of the EIS data using the following equation [75,76]:

$$D_{Na^+} = 0.5R^2T^2/S^2n^4F^4C^2\sigma^2,$$

where the Warburg factor σ refers the slope of the linear relationship between Z' and $\omega^{-1/2}$ and R, T, S, n, F, and C represent the gas constant, Kelvin temperature, electrode area, number of transferred electrons, Faraday constant, and concentration of Na^+, respectively. Accordingly, based on the fitted slopes by plotting Z' versus $\omega^{-1/2}$ (Fig. S8), the D_{Na^+} values of the $NiSe_2$, $NiSe_2$/C, 0.1Fe-$NiSe_2$/C, and 0.2Fe-$NiSe_2$/C electrodes can be obtained, and the corresponding variation trends of these electrodes at different cycles are illustrated in Fig. 7(e). For the 0.1Fe-$NiSe_2$/C electrode before cycling, the D_{Na^+} value was determined to be 4.3×10^{-12} cm^2 s^{-1}, which is approximately 16.5, 2.5, and 6.3 times higher than those of $NiSe_2$ (2.6×10^{-13} cm^2 s^{-1}), $NiSe_2$/C (1.7×10^{-12} cm^2 s^{-1}), and 0.2Fe-$NiSe_2$/C (6.8×10^{-13} cm^2 s^{-1}), respectively. As the cycling proceeded to 100 and 200 cycles, the D_{Na^+} value of 0.1Fe-$NiSe_2$/C monotonically increased from 4.3×10^{-12} cm^2 s^{-1} to 6.7×10^{-12} cm^2 s^{-1} and 8.7×10^{-12} cm^2 s^{-1}, while on the contrary, the D_{Na^+} values of the $NiSe_2$, $NiSe_2$/C, and 0.2Fe-$NiSe_2$/C electrodes gradually decayed to 2.2×10^{-14}, 1.3×10^{-12}, and 3.9×10^{-13} cm^2 s^{-1} after 100 cycles and further declined to 1.6×10^{-14}, 1.2×10^{-12}, and 3.1×10^{-13} cm^2 s^{-1} after 200 cycles, respectively. The in situ combination of porous carbon nanosheets and moderate Fe doping in $NiSe_2$ is proposed to provide more favorable fast ion diffusion channels in the flower-like structure, which can facilitate the rapid insertion/extraction of Na^+, thereby accounting for the excellent rate capability of the 0.1Fe-$NiSe_2$/C electrode. Notably, in the 0.2Fe-$NiSe_2$/C electrode, the ion transport kinetics quickly deteriorated compared to those of 0.1Fe-$NiSe_2$/C, demonstrating that a high Fe doping content in $NiSe_2$ might result in the agglomeration of active materials and impede the rapid diffusion of Na^+ in the hybrid composite.

To further evaluate the real application potential of 0.1Fe-$NiSe_2$/C as an anode, a full cell was constructed by pairing 0.1Fe-$NiSe_2$/C with a commercial rhombohedral $Na_3V_2(PO_4)_3$ (NVP) cathode, as schematically illustrated in Fig. 8(a). Fig. 8(b) shows the GCD curves of the device when tested at 1 A g^{-1} in an applied voltage window of 0.5–4 V [26,36]. In addition, the anode was presodiated in a half-cell at 0.5 A g^{-1} for 5 cycles to compensate for the large consumption of Na^+ in the electrolyte during the formation of SEI film and thereby improve the cycling stability. As shown in Fig. 8(c), our assembled full-cell device delivered initial charge/discharge capacities of 494 and 450 mAh g^{-1} at 1 A g^{-1}, suggest-

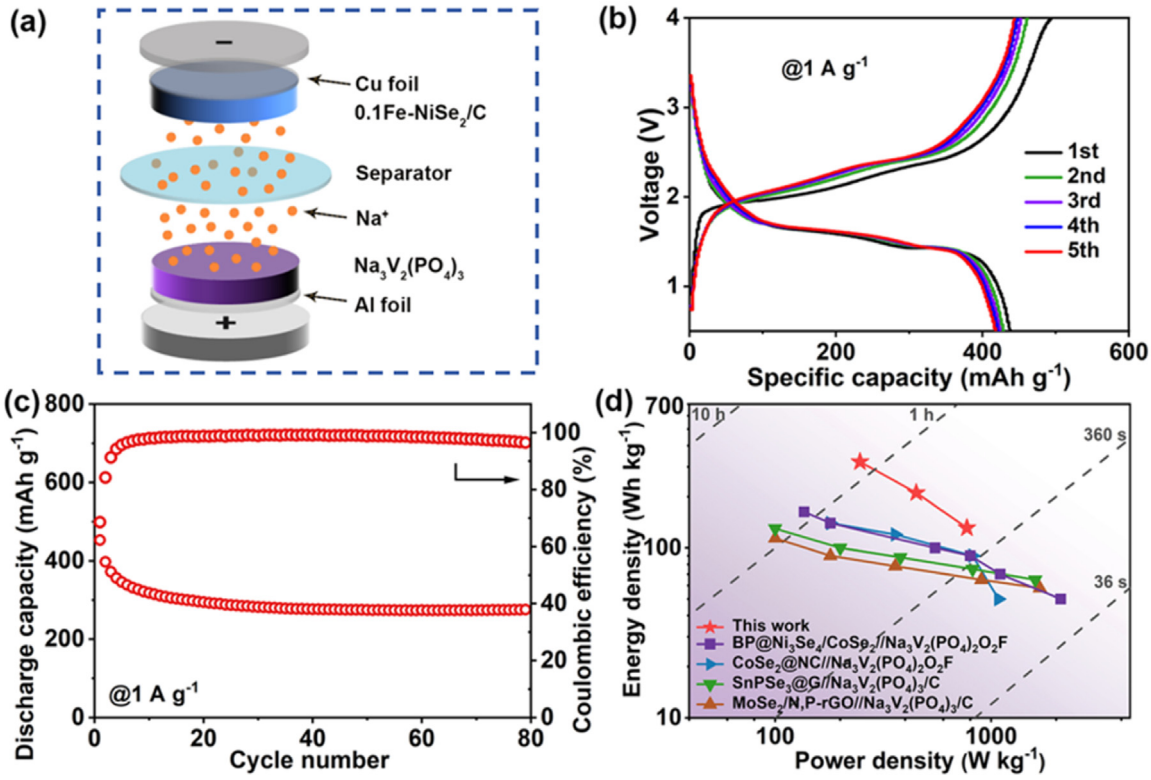

Fig. 8. Electrochemical performance of the 0.1Fe-$NiSe_2$/C//NVP full-cell device: (a) schematic diagram of the device, (b) GCD curves of the initial five cycles at 1 A g^{-1}, (c) cycling performance at 1 A g^{-1}, and (d) Ragone plots in comparison with other metal selenides reported in the literature.

ing a high ICE of 91.1%. The discharge capacity remained at 276 mAh g^{-1} after 80 cycles with a retention of 74.6% to the third cycle and CE approaching 100%, as shown in Fig. 8(c). Fig. 8(d) depicts the Ragone plot of the 0.1Fe-$NiSe_2$/C//NVP device, describing the relationship between the energy density and power density in comparison to those of recently reported metal-selenide-based SIBs. Remarkably, our device exhibited a maximum energy density of 321 Wh kg^{-1} at a power density of 247 W kg^{-1} and retained values as high as 131 Wh kg^{-1} at 772 W kg^{-1}, which are superior to those of previously reported full-cell devices, such as BP@Ni_3Se_4//$Na_3V_2(PO_4)_2O_2F$ [77], $CoSe_2$@NC//$Na_3V_2(PO_4)_2O_2F$ [78], $SnPSe_3$@G//NVP/C [79], and $MoSe_2$/N, P-rGO//NVP/C [80], demonstrating the good potential of 0.1Fe-$NiSe_2$/C toward real energy storage applications .

3. Conclusions

In summary, flower-like Fe-$NiSe_2$/C hybrid spheres were successfully prepared using an in situ glucose intercalation strategy through successive carbonization/selenization of Fe-Ni$(OH)_2$-G precursors derived from a facile one-pot hydrothermal method. Benefitting from the accelerated ion/electron transfer kinetics and reinforced structural integrity, the optimal anode composed of the 0.1Fe-$NiSe_2$/C hybrid spheres delivered an appreciable capacity, outstanding rate capability, and enhanced cycling stability. We believe that the strategy developed in this study will inspire more possibilities for the rational design and synthesis of novel high-capacity conversion-type transition-metal selenides for efficient sodium storage.

Declaration of Competing Interest

The authors declare that they have no known competing financial interests or personal relationships that could have appeared to influence the work reported in this paper.

CRediT authorship contribution statement

Cheng Liu: Conceptualization, Investigation, Validation, Writing – original draft. **Yi Wen:** Formal analysis, Investigation. **Gaoya Ren:** Data curation, Formal analysis, Investigation. **Yaxuan Li:** Data curation, Investigation, Validation. **Qianqian Sun:** Data curation, Formal analysis. **Shenghui Shen:** Resources, Visualization. **Zhujun Yao:** Funding acquisition, Validation. **Yefeng Yang:** Conceptualization, Funding acquisition, Resources, Supervision, Writing – review & editing.

Acknowledgements

The authors are grateful for the financial support provided by the Zhejiang Provincial Natural Science Foundation of China (Grant No. LY21E020010), National Natural Science Foundation of China (Grant No. 52102315), Shanxi-Zheda Institute of Advanced Materials and Chemical Engineering (2021SZ-TD006), and Science and Technology Program of Zhejiang University Institute of Wenzhou (Grant No. XMGL-KJZX-202206).

Supplementary materials

Supplementary material associated with this article can be found, in the online version, at doi:10.1016/j.chphma.2024.01.004.

References

[1] P.J. Wang, J.J. Huang, J. Zhang, L. Wang, P.H. Sun, Y.F. Yang, Z.J. Yao, Coupling hierarchical iron cobalt selenide arrays with N-doped carbon as advanced anodes for sodium ion storage, J. Mater. Chem. A 9 (2021) 7248–7256.
[2] L. Li, Y. Zheng, S. Zhang, J. Yang, Z. Shao, Z. Guo, Recent progress on sodium ion batteries: Potential high-performance anodes, Energy Environ. Sci. 11 (2018) 2310–2340.
[3] H.R. Yao, L. Zheng, S. Xin, Y.G. Guo, Air-stability of sodium-based layered-oxide cathode materials, Sci. China Chem. 65 (2022) 1076–1087.

[4] Z.Q. Lei, Y.J. Guo, E.H. Wang, W.H. He, Y.Y. Zhang, S. Xin, Y.X. Yin, Y.G. Guo, Layered oxide cathode-electrolyte interface towards Na-ion batteries: Advances and perspectives, Chem. Asian J. 17 (2022) e20220213.

[5] E. Wang, Y. Niu, Y.X. Yin, Y.G. Guo, Manipulating electrode/electrolyte interphases of sodium-ion batteries: Strategies and perspectives, ACS Mater. Lett. 3 (2021) 18–41.

[6] C. Luo, R. Qiu, G. Li, X. Shi, Z. Mao, R. Wang, J. Jin, B. He, Y. Gong, H. Wang, Electrospun $Na_3V_2(PO_4)_3$/carbon composite nanofibers as binder-free cathodes for advanced sodium-ion hybrid capacitors, Mater.Today Energy 30 (2022) 101148.

[7] E.M. Alhajji, J. Yin, J. Jin, M.N. Hedhili, U. Schwingenschlogl, H.N. Alshareef, Engineering of carbon anodes by laser irradiation for advanced sodium-ion batteries, Mater.Today Energy 38 (2023) 101404.

[8] T. Zhang, Z. Mao, X. Shi, J. Jin, B. He, R. Wang, Y. Gong, H. Wang, Tissue-derived carbon microbelt paper: A high-initial-coulombic-efficiency and low-discharge-platform K^+-storage anode for 4.5 V hybrid capacitors, Energy Environ. Sci. 15 (2022) 158–168.

[9] D. Yuan, Y. Dou, Y. Tian, D. Adekoya, L. Xu, S. Zhang, Robust pseudocapacitive sodium cation intercalation induced by cobalt vacancies at atomically thin $Co_{1-x}Se_2$/graphene heterostructure for sodium-ion batteries, Angew. Chem. Int. Ed. 60 (2021) 18830–18837.

[10] Y. Xiao, Y. Miao, S. Wan, Y.K. Sun, S. Chen, Synergistic engineering of Se vacancies and heterointerfaces in zinc-cobalt selenide anode for highly efficient Na-ion batteries, Small 18 (2022) 2202582.

[11] M.H. Han, E. Gonzalo, G. Singh, T. Rojo, A comprehensive review of sodium layered oxides: powerful cathodes for Na-ion batteries, Energy Environ. Sci. 8 (2015) 81–102.

[12] Z. Lv, M. Ling, M. Yue, X. Li, M. Song, Q. Zheng, H. Zhang, Vanadium-based polyanionic compounds as cathode materials for sodium-ion batteries: Toward high-energy and high-power applications, J. Energy Chem. 55 (2021) 361–390.

[13] K. Hurlbutt, S. Wheeler, I. Capone, M. Pasta, Prussian blue analogs as battery materials, Joule 2 (2018) 1950–1960.

[14] G. Ke, H. Chen, J. He, X. Wu, Y. Gao, Y. Li, H. Mi, Q. Zhang, C. He, X. Ren, Ultrathin MoS_2 anchored on 3D carbon skeleton containing SnS quantum dots as a high-performance anode for advanced lithium ion batteries, Chem. Eng. J. 403 (2021) 126251.

[15] L. Yao, Q. Gu, X. Yu, Three-dimensional MOFs@MXene aerogel composite derived MXene threaded hollow carbon confined CoS nanoparticles toward advanced alkali-ion batteries, ACS Nano 15 (2021) 3228–3240.

[16] Y.T. Gong, Y. Li, Y. Li, M.Q. Liu, Y. Bai, C. Wu, Metal selenides anode materials for sodium ion batteries: Synthesis, modification, and application, Small 19 (2022) 2370019.

[17] G. Fang, Q. Wang, J. Zhou, Y. Lei, Z. Chen, Z. Wang, A. Pan, S. Liang, Metal organic framework-templated synthesis of bimetallic selenides with rich phase boundaries for sodium-ion storage and oxygen evolution reaction, ACS Nano 13 (2019) 5635–5645.

[18] J. Feng, S.H. Luo, S.X. Yan, Y. Zhan, Q. Wang, Y.H. Zhang, X. Liu, L.J. Chang, Hierarchically nitrogen-doped carbon wrapped $Ni_{0.6}Fe_{0.4}Se_2$ binary-metal selenide nanocubes with extraordinary rate performance and high pseudocapacitive contribution for sodium-ion anodes, J. Mater. Chem. A 9 (2021) 1610–1622.

[19] J. Feng, S.H. Luo, S.X. Yan, Y. Zhan, Q. Wang, Y.H. Zhang, X. Liu, L.J. Chang, Rational design of yolk-shell Zn-Co-Se@N-doped dual carbon architectures as long-life and high-rate anodes for half/full Na-ion batteries, Small 17 (2021) 2101887.

[20] J. Feng, S.H. Luo, Y. Zhan, S.X. Yan, P.W. Li, L. Zhang, Q. Wang, Y.H. Zhang, X. Liu, Ingeniously designed yolk-shell-structured $FeSe_2$@NDC nanoboxes as an excellent long-life and high-rate anode for half/full na-ion batteries, ACS Appl. Mater. Interfaces 13 (2021) 51095–51106.

[21] J. Feng, S.H. Luo, Y.C. Lin, Y. Zhan, S.X. Yan, P.Q. Hou, Q. Wang, Y.H. Zhang, Metal-organic framework derived $CoSe_2$/N-doped carbon core-shell nanoparticles encapsulated in porous N-doped carbon nanotubes as high-performance anodes for sodium-ion batteries, J. Power Sources 535 (2022) 231444.

[22] Z. Zheng, H.H. Wu, H. Liu, Q. Zhang, X. He, S. Yu, V. Petrova, J. Feng, R. Kostecki, P. Liu, D.L. Peng, M. Liu, M.S. Wang, Achieving fast and durable lithium storage through amorphous FeP nanoparticles encapsulated in ultrathin 3D P-doped porous carbon nanosheets, ACS Nano 14 (2020) 9545–9561.

[23] X. Ge, Z. Li, L. Yin, Metal-organic frameworks derived porous core/shell CoP@C polyhedrons anchored on 3D reduced graphene oxide networks as anode for sodium-ion battery, Nano Energy 32 (2017) 117–124.

[24] S.H. Zhu, Q.D. Li, Q.L. Wei, R.M. Sun, X.Q. Liu, Q.Y. An, L.Q. Mai, $NiSe_2$ nanooctahedra as an anode material for high-rate and long-life sodium-ion battery, ACS Appl. Mater. Interfaces 9 (2017) 311–316.

[25] H.S. Fan, H. Yu, X.L. Wu, Y. Zhang, Z.Z. Luo, H.W. Wang, Y.Y. Guo, S. Madhavi, Q.Y. Yan, Controllable preparation of square nickel chalcogenide (NiS and $NiSe_2$) nanoplates for superior Li/Na ion storage properties, ACS Appl. Mater. Interfaces 8 (2016) 25261–25267.

[26] L. Yu, L.Y. Shao, S.G. Wang, J.D. Guan, X.Y. Shi, J.J. Cai, N. Tarasenko, Z.P. Sun, A low-cost $NiSe_2$ derived from waste nickel foam as a high-performance anode for sodium ion batteries, Mater. Today Phys. 22 (2022) 100593.

[27] Z. Liang, H. Tu, K. Zhang, Z. Kong, M. Huang, D. Xu, S. Liu, Y. Wu, X. Hao, Self-supporting $NiSe_2$@BCNNTs electrode for high-performance sodium ion batteries, Chem. Eng. J. 437 (2022) 135421.

[28] H. Fan, H. Yu, X. Wu, Y. Zhang, Z. Luo, H. Wang, Y. Guo, S. Madhavi, Q. Yan, Controllable preparation of square nickel chalcogenide (NiS and $NiSe_2$) nanoplates for superior Li/Na ion storage properties, ACS Appl. Mater. Interfaces 8 (2016) 25261–25267.

[29] L. Wang, C. Lin, T. Liang, N. Wang, J. Feng, W. Yan, $NiSe_2$ nanoparticles encapsulated in CNTs covered and N-doped TiN/carbon nanofibers as a binder-free anode for advanced sodium-ion batteries, Mater. Today Chem. 24 (2022) 100849.

[30] C. Liu, M.X. Lu, Q.Q. Sun, S.Q. Jiang, X.Y. Li, Z.J. Yao, T.C. Liu, Z.Z. Ye, Y.F. Yang, $NiSe_2$ nanoparticles decorated on carbon nanosheet arrays as anodes for sodium storage, ACS Appl. Nano Mater. 5 (2022) 13498–13508.

[31] S.T. Liu, D. Li, G.J. Zhang, D.D. Sun, J.S. Zhou, H.H. Song, Two-dimensional $NiSe_2$/N-rich carbon nanocomposites derived from Ni-hexamine frameworks for superb Na-ion storage, ACS Appl. Mater. Interfaces 10 (2018) 34193–34201.

[32] Z.X. Yuan, H.N. Guo, Y.K. Huang, W.Q. Li, Y.F. Liu, K. Chen, M.Y. Yue, Y.J. Wang, Composites of $NiSe_2$@C hollow nanospheres wrapped with $Ti_3C_2T_x$ MXene for synergistic enhanced sodium storage, Chem. Eng. J. 429 (2022) 132394.

[33] X. Xia, D.Y. Zhang, S.Y. Gao, B. Yang, X.X. Meng, Y.L. He, B. Wang, Z.Y. Han, K.J. Wang, Porous corallite-like $NiSe_2$/CNTs nanocomposite fabricated by a convenient one-step in-suit solid-phase synthesis method with high performance in both supercapacitor and sodium-ion battery, J. Alloys Compd. 958 (2023) 170364.

[34] X. Ou, J. Li, F.H. Zheng, P. Wu, Q.C. Pan, X.H. Xiong, C.H. Yang, M.L. Liu, In situ X-ray diffraction characterization of $NiSe_2$ as a promising anode material for sodium ion batteries, J. Power Sources 343 (2017) 483–491.

[35] S.W. Fan, G.D. Li, J.Y. Liu, Two-dimensional fence-like Co-doped $NiSe_2$/C nanosheets as an anode for half/full sodium-ion batteries, Inorg. Chem. Front. 8 (2021) 100–108.

[36] J. Liu, J. Xie, H.L. Dong, H.X. Wei, C.C. Sun, J. Yang, H.B. Geng, Iron doping of $NiSe_2$ nanosheets to accelerate reaction kinetics in sodium-ion half/full batteries, Sci. China Chem. 66 (2023) 69–78.

[37] H. Wu, K. Wang, M.J. Li, Y.T. Wang, Z. Zhu, Z.Z.Du JialeLiang, W. Ai, S. He, R.L. Yuan, B.W. Wang, P. He, J.S. Wu, Double-walled NiTeSe-$NiSe_2$ nanotubes anode for stable and high-rate sodium-ion batteries, Small 19 (2023) 2300162.

[38] S.Y. Lu, H. Wu, J.W. Hou, L.M. Liu, J. Li, C.J. Harris, C.Y. Lao, Y.Z. Guo, K. Xi, S.J. Ding, G.X. Gao, A.K. Cheetham, R.V. Kumar, Phase boundary engineering of metal-organic-framework-derived carbonaceous nickel selenides for sodium-ion batteries, Nano Res. 13 (2020) 2289–2298.

[39] H. Zheng, J.Y. Wang, H.W. Li, S.Q. Deng, Y.Z. Zuo, W. Yan, J.J. Zhang, Constructing a novel heterostructure of $NiSe_2$/$CoSe_2$ nanoparticles with boosted sodium storage properties for sodium-ion batteries, J. Mater. Chem. A 10 (2022) 16268–16279.

[40] Q. Sun, Y. Wen, S. Jiang, X. Li, Z. Yao, T. Liu, S. Shen, Y. Yang, Coupling of $NiSe_2$ with $MoSe_2$ confined in nitrogen-doped carbon spheres as anodes for fast and durable sodium storage, J. Alloys Compd. 944 (2023) 169157.

[41] Y. Xiang, Q.P. Li, X.J. Wei, X.Y. Li, Q.J. Zheng, Y. Huo, D.M. Lin, Constructing NiS_2/$NiSe_2$ heteroboxes with phase boundaries for sodium-ion batteries, J. Colloid Interface Sci. 607 (2022) 752–759.

[42] L. Gao, H.B. Ren, X.J. Lu, S.W. Joo, T.X. Liu, J.R. Huang, Heterostructure of $NiSe_2$/MnSe nanoparticles distributed on cross-linked carbon nanosheets for high--performance sodium-ion battery, Appl. Surf. Sci. 599 (2022) 154067.

[43] Y. Li, M. Chen, B. Liu, Y. Zhang, X. Liang, X. Xia, Heteroatom doping: An effective way to boost sodium ion storage, Adv. Energy Mater. 10 (2020) 2000927.

[44] Y. He, M. Luo, C. Dong, X. Ding, C. Yin, A. Nie, Y. Chen, Y. Qian, L. Xu, Coral-like $Ni_xCo_{1-x}Se_2$ for Na-ion battery with ultralong cycle life and ultrahigh rate capability, J. Mater. Chem. A 7 (2019) 3933–3940.

[45] W. Quan, Y. Xu, Y. Wang, S. Meng, D. Jiang, M. Chen, Hierarchically structured Co_3O_4@glucose-modified LDH architectures for high-performance supercapacitors, Appl. Surf. Sci. 488 (2019) 639–647.

[46] L. Lv, K. Xu, C. Wang, H. Wan, Y. Ruan, J. Liu, R. Zou, L. Miao, K. Ostrikov, Y. Lan, J. Jiang, Intercalation of glucose in NiMn-layered double hydroxide nanosheets: An effective path way towards battery-type electrodes with enhanced performance, Electrochim. Acta 216 (2016) 35–43.

[47] V. Rives, M. del Arco, C. Martin, Intercalation of drugs in layered double hydroxides and their controlled release: A review, Appl. Clay Sci. 88-89 (2014) 239–269.

[48] C. Chakraborty, K. Dana, S. Malik, Intercalation of perylenediimide dye into LDH clays: Enhancement of photostability, J. Phys. Chem. C 115 (2011) 1996–2004.

[49] Q. Liu, P. Zhang, Z. Wang, S. Liu, X. Ren, K. Qian, X. Chen, J. Li, J. Yao, Y. Gan, L. Lv, H. Wan, H. Wang, Glucose pillared Ni-Co layered double hydroxide clay materials toward durable cathodes for alkaline zinc batteries, J. Alloys Compd. 963 (2023) 171227.

[50] L. Yang, Z. Liu, S. Zhu, L. Feng, W. Xing, Ni-based layered double hydroxide catalysts for oxygen evolution reaction, Mater. Today Phys. 16 (2021) 100292.

[51] Y. Chen, B. Qu, L. Hu, Z. Xu, Q. Li, T. Wang, High-performance supercapacitor and lithium-ion battery based on 3D hierarchical NH_4F-induced nickel cobaltate nanosheet-nanowire cluster arrays as self-supported electrodes, Nanoscale 5 (2013) 9812–9820.

[52] P. Upale, S. Verma, S.B. Ogale, Superior oxygen evolution reaction performance of NiCoFe spinel oxide nanowires in situ grown on beta-$Ni(OH)_2$ nanosheet-decorated Ni foam: case studies on stoichiometric and off-stoichiometric oxides, J. Mater. Chem. A 11 (2023) 8972–8987.

[53] S. Hu, Y. Li, D. Kim, M. Liu, L.Y.S. Lee, K.Y. Wong, Surface modulated Fe doping of beta-$Ni(OH)_2$ nanosheets for highly promoted oxygen evolution electrocatalysis, Ecomat 4 (2022) e12256.

[54] Y. Liu, Z. Yang, Y. Zou, S. Wang, J. He, Trace cobalt doping and defect engineering of high surface area alpha-$Ni(OH)_2$ for electrocatalytic urea oxidation, Energy Environ. Mater. (2023) e12576.

[55] X. Wang, H.L, P.V.P, A.C.M, E.M, Studies of the performance of nanostructural multiphase nickel hydroxide, J. Power Sources 115 (2003) 153–160.

[56] P.H.L.N.M. Wehrens-Dijksma, Electrochemical quartz microbalance characterization of $Ni(OH)_2$-based thin film electrodes, Electrochim. Acta 51 (2006) 3609–3621.

[57] M. Lu, X.P. Yuan, X.H. Guan, G.S. Wang, Synthesis of nickel chalcogenide hollow spheres using an L-cysteine-assisted hydrothermal process for efficient supercapacitor electrodes, J. Mater. Chem. A 5 (2017) 3621–3627.

[58] J.J. Ye, Z.Z. Chen, Z.Q. Zheng, Z.H. Fu, G.H. Gong, G. Xia, C. Hu, Rationally designed hollow carbon nanospheres decorated with S,P co-doped $NiSe_2$ nanoparticles for high-performance potassium-ion and lithium-ion batteries, J. Energy Chem. 78 (2023) 401–411.
[59] J.H. Choi, S.K. Park, Y.C. Kang, A salt-templated strategy toward hollow iron selenides-graphitic carbon composite microspheres with interconnected multicavities as high-performance anode materials for sodium-ion batteries, Small 15 (2019) 1803043.
[60] P. Ge, H. Hou, S. Li, L. Yang, X. Ji, Tailoring rod-like $FeSe_2$ coated with nitrogen–doped carbon for high-performance sodium storage, Adv. Funct. Mater. 28 (2018) 1801765.
[61] W. Zhong, W. Tang, Y. Wu, Y. Zhang, Y. Qi, S.J. Bao, X. Zhang, M. Xu, Heterogeneous interface designing of bimetallic selenides nanocubes for superior sodium storage, J. Power Sources 506 (2021) 230249.
[62] Z. Ali, M. Asif, T. Zhang, X. Huang, Y. Hou, General approach to produce nanostructured binary transition metal selenides as high-performance sodium ion battery anodes, Small 15 (2019) 1901995.
[63] C. An, Y. Yuan, B. Zhang, L. Tang, B. Xiao, Z. He, J. Zheng, J. Lu, Graphene wrapped $FeSe_2$ nano-microspheres with high pseudocapacitive contribution for enhanced Na-ion storage, Adv. Energy Mater. 9 (2019) 1900356.
[64] H.J. Qiu, Y. Ito, W. Cong, Y. Tan, P. Liu, A. Hirata, T. Fujita, Z. Tang, M. Chen, Nanoporous graphene with single-atom nickel dopants: An efficient and stable catalyst for electrochemical hydrogen production, Angew. Chem. Int. Ed. 54 (2015) 14031–14035.
[65] X. Lin, S. Wang, W. Tu, H. Wang, Y. Hou, W. Dai, R. Xu, Magnetic hollow spheres assembled from graphene-encapsulated nickel nanoparticles for efficient photocatalytic CO_2 reduction, ACS Appl. Energy Mater. 2 (2019) 7670–7678.
[66] L. Wang, X. Wang, S. Xi, Y. Du, J. Xue, Alpha-$Ni(OH)_2$ originated from electro-oxidation of $NiSe_2$ supported by carbon nanoarray on carbon cloth for efficient water oxidation, Small 15 (2019) 1902222.
[67] T. Hu, Z. Jiang, Z. Fu, Z.J. Jiang, A NiFe/$NiSe_2$ heterojunction bifunctional catalyst rich in oxygen vacancies introduced using dielectric barrier discharge plasma for liquid and flexible all-solid-state rechargeable Zn-air batteries, J. Mater. Chem. A 10 (2022) 8739–8750.
[68] Z. Li, L. Zhang, X. Ge, C. Li, S. Dong, C. Wang, L. Yin, Core-shell structured CoP/FeP porous microcubes interconnected by reduced graphene oxide as high performance anodes for sodium ion batteries, Nano Energy 32 (2017) 494–502.
[69] J. Xia, L. Liu, S. Jamil, J. Xie, H. Yan, Y. Yuan, Y. Zhang, S. Nie, J. Pan, X. Wang, G. Cao, Free-standing SnS/C nanofiber anodes for ultralong cycle-life lithium-ion batteries and sodium-ion batteries, Energy Storage Mater. 17 (2019) 1–11.
[70] H. Xia, L. Zan, P. Yuan, G. Qu, H. Dong, Y. Wei, Y. Yu, Z. Wei, W. Yan, J.S. Hu, D. Deng, J.N. Zhang, Evolution of stabilized 1T-MoS_2 by atomic-interface engineering of 2H-MoS_2/Fe-N-x towards enhanced sodium ion storage, Angew. Chem. Int. Ed. 135 (2023) e202218282.
[71] J. Sang, X. Zhang, K. Liu, G. Cao, R. Guo, S. Zhang, Z. Wu, Y. Zhang, R. Hou, Y. Shen, G. Shao, Effective coupling of amorphous selenium phosphide with high-conductivity graphene as resilient high-capacity anode for sodium-ion batteries, Adv. Funct. Mater. 33 (2023) 2211640.
[72] Z. Cao, J. Cui, D. Yu, Y. Wang, J. Liu, J. Zhang, J. Yan, Y. Zhang, S. Sun, Y. Wu, Synergistic engineering of architecture and composition in bimetallic selenide@carbon hybrid nanotubes for enhanced lithium- and sodium-ion batteries, Adv. Funct. Mater. 33 (2023) 2306862.
[73] X. Xiao, W. Yao, T. Yan, W. Zhang, Q. Zhang, S. Zhong, Z. Yan, Hybrid CuSn nanosphere-functionalized Cu/Sn co-doped hollow carbon nanofibers as anode materials for sodium-ion batteries, Nanoscale 15 (2023) 15405–15414.
[74] Y.Y. Zheng, X.R. Kong, L. He, Y. Song, Y. Zhao, A solid-state Matryoshka doll–like microwave method for one-step rapid synthesis of composites of $NiSe_2$ and nitrogen-doped porous carbon for sodium storage, J. Mater. Chem. C 10 (2022) 18052–18062.
[75] T. Tang, G. Ren, Y. Wen, M. Lu, Z. Yao, T. Liu, S. Shen, H. Xie, X. Xia, Y. Yang, Spatially confined Fe_7S_8 nanoparticles anchored on a porous nitrogen-doped carbon nanosheet skeleton for high-rate and durable sodium storage, ACS Appl. Mater. Interfaces 15 (2023) 30249–30261.
[76] M.X. Lu, C. Liu, Q.Q. Sun, G.Y. Ren, Y.X. Li, Y.T. Wang, J.Y. Gao, Z.J. Yao, Y.F. Yang, Ion-exchange route induced heterostructured CoS_2/FeS nanoparticles confined in hollow N-doped carbon frameworks for enhanced sodium storage performance, ACS Appl. Nano Mater. 6 (2023) 11944–11954.
[77] J. Yang, C. Zhang, J. Geng, Y. Sui, H. Wei, C. Sun, H. Geng, Y. Liu, Nickel cobalt selenides on black phosphorene with fast electron transport for high-energy density sodium-ion half/full batteries, Inorg. Chem. Front. 10 (2023) 424–434.
[78] J. Geng, C. Sun, J. Xie, H. Dong, Z. Wang, H. Wei, Y. Cheng, Y. Tian, H. Geng, Topological transformation construction of a $CoSe_2$/N-doped carbon heterojunction with a three-dimensional porous structure for high-performance sodium-ion half/full batteries, Inorg. Chem. Front. 9 (2022) 3176–3186.
[79] X. Ren, Y. Zhao, Q. Li, F. Cheng, W. Wen, L. Zhang, Y. Huang, X. Xia, X. Li, D. Zhu, K. Huo, R. Tai, A novel multielement nanocomposite with ultrahigh rate capacity and durable performance for sodium-ion battery anodes, J. Mater. Chem. A 8 (2020) 11598–11606.
[80] F. Niu, J. Yang, N. Wang, D. Zhang, W. Fan, J. Yang, Y. Qian, $MoSe_2$-covered N,P-doped carbon nanosheets as a long-life and high-rate anode material for sodium-ion batteries, Adv. Funct. Mater. 27 (2017) 1700522.